Korean J. Chem. Eng., 34(6), 1669-1677 (2017)
DOI: 10.1007/s11814-017-0073-6

pISSN: 0256-1115
eISSN: 1975-7220

Effective photoconversion of CO_2 into CH_4 over $Ti_{30}Si_{70}$MCM-41 nanoporous catalyst photosensitized by a ruthenium dye

Younghwan Im, Jae Hyung Lee, and Misook Kang†

Department of Chemistry, College of Natural Sciences, Yeungnam University, Gyeongsan, Gyeongbuk 38541, Korea
(*Received 16 January 2017 • accepted 13 March 2017*)

Abstract−Nanoporous $Ti_{30}Si_{70}$MCM-41 was applied as a photocatalyst for effective reduction of CO_2 to CH_4. A ruthenium dye (N_{719}) was also introduced onto the surface of $Ti_{30}Si_{70}$MCM-41 as a photosensitizer to improve its photoabsorption in the visible range. The catalytic performance of N_{719}-photosensitized $Ti_{30}Si_{70}$MCM-41 was superior to that of the non-photosensitized $Ti_{30}Si_{70}$MCM-41 and N_{719}-photosensitized $Ti_{30}Si_{70}O_{200}$ nanomaterials. The photoreduction of CO_2 to CH_4 was remarkably improved on N_{719}-(5 h)-photosensitized $Ti_{30}Si_{70}$MCM-41, with a production of 1,900 μmol g_{cat}^{-1} L^{-1} after an 8 h reaction. The results were attributed to the effective charge separation and the inhibited recombination of photogenerated electron-hole pairs on N_{719}-photosensitized $Ti_{30}Si_{70}$MCM-41. Lastly, a model for the enhanced photoactivity over N_{719}-photosensitized $Ti_{30}Si_{70}$MCM-41 was proposed.

Keywords: Ruthenium Dye, N_{719}-photosensitized-$Ti_{30}Si_{70}$MCM-41, CO_2 Photoreduction, CH_4 Production, Nanoporous, Recombination of Electron-hole Pairs

INTRODUCTION

Carbon dioxide, which constitutes up to 70% of total emissions of greenhouse gases, has been an important issue in global economics and politics, as well as the environment. Various physical or chemical processes for removing and utilizing carbon dioxide have been introduced [1,2]. In particular, methane production via the photocatalytic reduction of CO_2 is a hot research topic in the CO_2 utilization field [3,4]. This method is environmentally friendly, and the photocatalytic reduction of CO_2 with H_2O is essential for the development of a solar-energy-based, carbon-neutral cycle. CO_2 photoreduction research has focused on titanium dioxide (TiO_2)-based nanomaterials because of their nontoxicity, chemical stability, and natural abundance [5-7]. However, the large band gap of TiO_2 of 3.2 eV limits its absorption in the ultraviolet (UV) region. To improve its photocatalytic efficiency, intensive research on extending the absorption range of TiO_2 to the visible regions has been conducted, which has included combining it with other metal semiconductors [8-12] or functionalizing its surface with dye molecules [13,14], such as ruthenium poly-pyridyl dyes, to achieve rapid photoinduced electron injection into its conduction band. In particular, dye-functionalized semiconductor materials can absorb light in the visible region, resulting in effective photoreactions. Benko et al. [15] reported electron injection from the transition metal complex $Ru(dcbpy)_2(NCS)_2$ (dcbpy: 4,4′-dicarboxy-2,2′-bipyridine) to a TiO_2 nanocrystalline film, which suggests that dyes with a higher-state redox potential are also capable of electron injection to below the conduction band edge of a semiconductor when excited by sufficiently energetic photons. Fuldner et al. [16] reported that nitrobenzene can be reduced cleanly to aniline using Ru-sensitized TiO_2 photocatalysts. Theil et al. [17] showed that Ru-dye-sensitized Au-SiO_2@TiO_2 and Au/Pt-SiO_2@TiO_2 assemblies had first-order rate constants up to 52% higher than those of the corresponding nanostructures without further dye functionalization. On the other hand, the use of mesoporous network structures, such as Ti-incorporated MCM or the SBA series, has been reported to enhance the adsorption of the reactive species and the utilization of incident light, and thereby increase the photocatalytic activity [18-20]. In our previous study [21], well-ordered nanoporous $TiSiO_2$ exhibited a high CH_4 production efficiency via CO_2 photoreduction. The remarkable performance of nanoporous TiO_2 in CO_2 photoreduction probably benefits from the confined space effect of the ordered nanoporous structure, particularly in cases using alkaline earth metals, such as Ca, to increase the absorption of CO_2. On the other hand, TiO_2 exhibited a CH_4 conversion of lower than 2.0 μmol g_{cat}^{-1} h^{-1}. Therefore, various approaches are necessary to develop new catalytic systems to improve CH_4 production.

In this study we examined whether dye molecules are well linked to the regular surfaces of nanoporous TiO_2 particles, exhibit good absorption of visible light despite its lower photon energy, and are capable of facilitating electron-hole charge separation in a semiconductor. The dye molecules act as a photosensitizer to inject photoexcited electrons into the TiO_2 nanoporous semiconductor. The nanoporous TiO_2 particles prolong the lifetime of the charge-separated state by acting as electrons or hole traps, and thereby enhance the carrier separation and photocatalytic activity [22,23]. Therefore, this study evaluated the synergistic effects of nanoporous TiO_2 and a ruthenium dye molecule (N_{719}). To maximize the CO_2 absorption capacity, nanoporous $Ti_{30}Si_{70}$MCM-41, in which Ti ions partially substituted for Si sites in the SiMCM-41 framework, was synthesized using a conventional hydrothermal treatment. The resulting nanoporous N_{719}-photosensitized $Ti_{30}Si_{70}$MCM-41 was applied

†To whom correspondence should be addressed.
E-mail: mskang@ynu.ac.kr

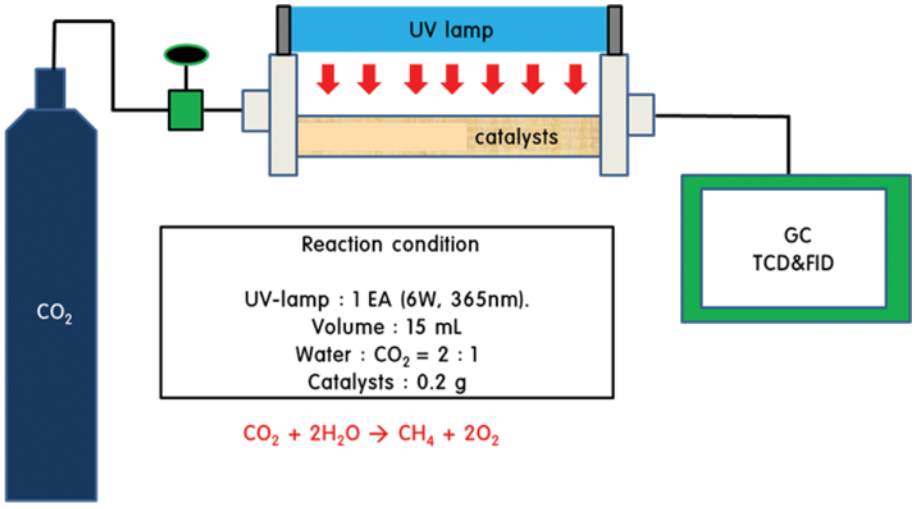

Fig. 1. Schematic diagram of the laboratory-designed, batch-type reactor for CO_2 photoreduction.

to the photoreduction of CO_2 to CH_4, and the results were compared with that on the N_{719}-photosensitized $Ti_{30}Si_{70}$ nanomaterial. $Ti_{30}Si_{70}$MCM-41 was examined using X-ray diffraction (XRD), transmission electron microscopy (TEM), Brunauer-Emmett-Teller (BET) surface area, and cyclic voltammetry (CV) measurements. The N_{719}-photosensitized samples were then characterized using ultraviolet-visible (UV-vis) spectroscopy.

MATERIALS AND METHODS

1. Synthesis and Characterization of $Ti_{30}Si_{70}$MCM-41 and N_{719}-(x h)-photosensitized $Ti_{30}Si_{70}$MCM-41

MCM-41 was synthesized hydrothermally according to our previous study [21] and as reported in the literature [24,25]. The composition of sol solution was $6.0SiO_2 : 1.0CTABr : 0.15(NH_4)_2O : 350H_2O$. The final solution was prepared by heating at 100 °C for 24 h in an autoclave. After synthesis, the resulting powder was thermal treated at 550 °C for 5 h in air and is termed SiMCM-41 herein. Then, silicon sites were replaced with titanium ions (titanium tetraisopropoxide, Junsei Co.) in the nanoporous framework. We previously determined the optimal Ti content to be 30% of the silicon content (i.e., Ti : Si molar ratio=3 : 7) [21], and the resulting solid, termed $Ti_{30}Si_{70}$MCM-41, was used in the present study. In the final step, dye functionalization was conducted using a dipping method. $Ti_{30}Si_{70}$MCM-41 powders were added to 30.0 mL of an ethanol solution containing 0.5 mM dye (ruthenium dye, N_{719}, Solaronix Co.). The dye adsorption times were varied (0, 1, 3, 5, and 24 h), and afterwards, the powders were washed with deionized water and dried at 60 °C for 24 h in an oven. The final samples are termed N_{719}-(x h)-photosensitized $Ti_{30}Si_{70}$MCM-41.

The synthesized $Ti_{30}Si_{70}$MCM-41 powder was examined using XRD (MPD, PANalytical) using nickel-filtered CuKα radiation (40 kV, 40 mA). The morphology of the particles was examined using TEM (JEOL 2000EX) and the atomic composition of the film was analyzed by energy-dispersive X-ray spectroscopy (EDAX, EX-250, Horiba) at 120 kV. The BET surface areas of the catalysts were tested using a Belsorp II instrument. The reflectance UV-vis spectra of the N_{719}-(x h)-photosensitized $Ti_{30}Si_{70}$MCM-41 powders were attained using a Cary 500 spectrometer with a reflectance sphere in the 200-800 nm range. The photocurrent densities were measured using an electrochemical station (CompactStat, Ivium Tech.) in three-electrode mode in a 1.0 M NaOH aqueous solution using an AM 1.5 solar simulator (ABE Tech.) as the light source. A platinum wire and Ag/AgCl electrode were, respectively, used as the counter and reference electrode. The adsorption ability of the catalysts for CO_2 gas was measured from CO_2-temperature programmed desorption (TPD) experiments in the same manner using BELCAT (Bel Japan Inc., Japan).

2. Photocatalytic Activity Test over the N_{719}-(x h)-photosensitized $Ti_{30}Si_{70}$MCM-41 Catalysts

Fig. 1 shows a schematic diagram of the batch-type photoreactor designed in the laboratory. The reactor consists of a rectangular quartz cell with a total volume of 15.0 mL. The photocatalytic activity was examined using 0.20 g of powdered N_{719}-(x h)-photosensitized $Ti_{30}Si_{70}$MCM-41 catalysts distributed uniformly at the bottom of the reaction chamber. A 1.0 mm thick quartz glass window cover was settled on top of the reactor to enable the effective transfer of radiation from a 6.0 W/cm^2 mercury lamp with a wavelength of 365 nm. The reactor was checked by purging with helium carrier gas. The CO_2 concentration was adjusted using helium (99.99%) as the diluent gas. The reaction temperature and pressure were kept at 30 °C and 1.0 atm. Before starting the experiment, the reactor was purged for 1 h with a mixture of CO_2 and helium. The $CO_2 : H_2O$ ratio was fixed at 1 : 2. During the photocatalysis process, the product mixture was sampled off-line by using a gas-tight syringe (Agilent, 250 μm) with the same volume, and determined by a gas chromatograph (GC, iGC7200, Donam Co., Korea) equipped with a thermal conductivity detector (TCD) and a flame ionization detector (FID). First, the gaseous products produced by the in-situ system were introduced into the TCD, which was connected to a Carboxen 1000 (Young Lin Instrument Co., Korea) column, to measure the light gases (H_2, O_2, and CO), and the extracted gases were then introduced into the FID to separate the C_1 (methane)-C_3 light hydrocarbons, as well as the oxygenated compounds,

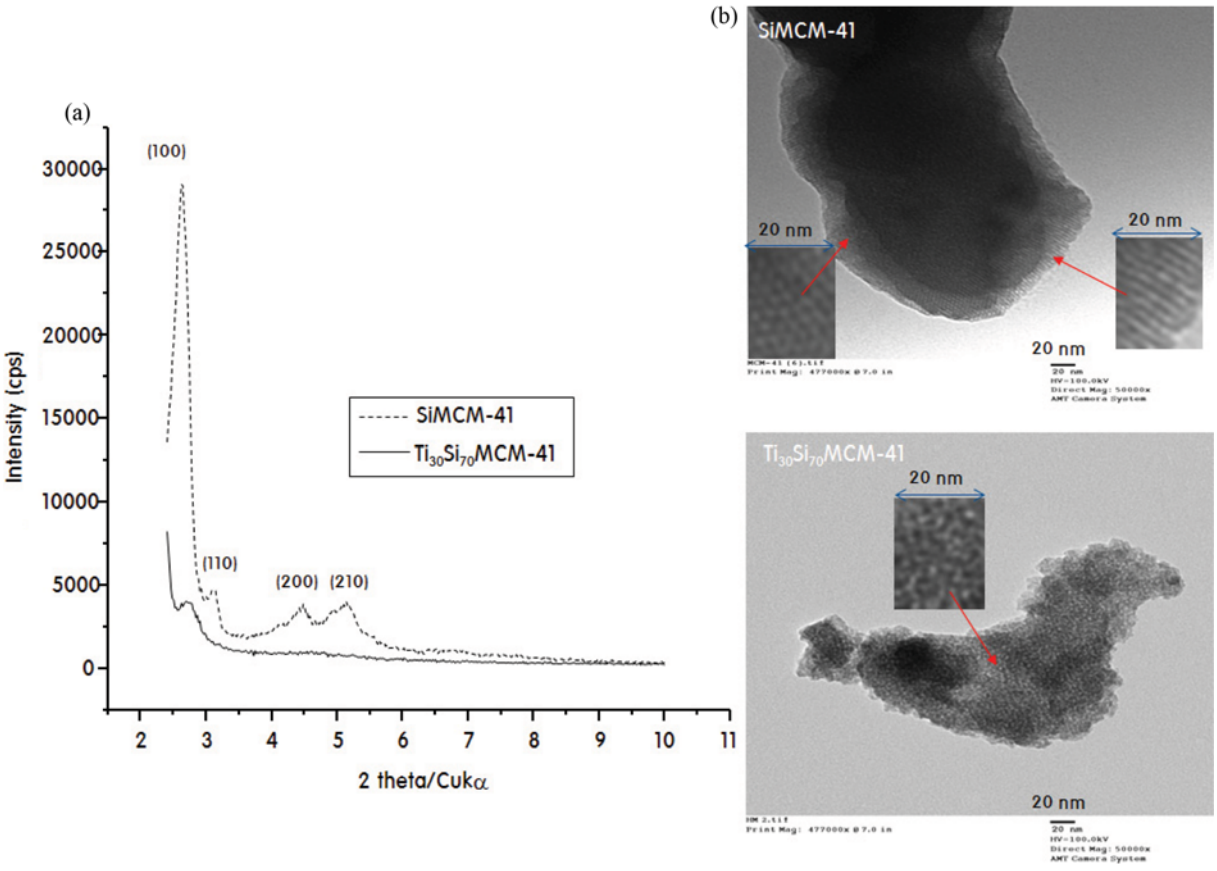

Fig. 2. XRD patterns (a) and TEM images (b) of the prepared SiMCM-41 and $Ti_{30}Si_{70}$MCM-41 powders.

such as methanol, acetaldehyde, and formic acid. The product selectivity was calculated with the following equation: $C_i(\%)=C_i$ moles in product/total moles of C produced 100.

RESULTS AND DISCUSSION

1. Physical Properties of the Synthesized $Ti_{30}Si_{70}$MCM-41 Powders

Fig. 2(a) and (b) show the XRD patterns and TEM images of the prepared SiMCM-41 and $Ti_{30}Si_{70}$MCM-41 powders. In Fig. 2(a), a shape reflection peak corresponding to the (100) plane is observed at a low angle ($2\theta=2^{\circ}$-2.5°) in SiMCM-41, indicating the typical hexagonal SiMCM-41 structure [26]. In addition, three reflection peaks, which were indexed to the (110), (200), and (210) planes, are clearly visible at $2\theta=3^{\circ}$-7° in the XRD patterns of the SiMCM-41 sample. The presence of well-defined XRD peaks indicated the highly ordered structure of the nanoporous molecular sieves. In contrast, the peak of the interplanar spacing, d_{100}, decreases with increasing Ti content, but the peak signal remains until 30 mol% Ti insertion. The peak broadening in the $Ti_{30}Si_{70}$MCM-41 sample was attributed to the smaller crystalline due to slow crystal growth by the insertion of many titanium ions, which are larger than silicon ions, into the SiMCM-41 framework. This could be related to the probable incorporation of Ti atoms into the silica framework. The substitution of Si^{4+} with Ti^{4+} distorts the geometry around Ti from ideal tetrahedral coordination because the ionic radius of Ti^{4+} (0.068 nm) is larger than that of Si^{4+} (0.041 nm). Fig. 2(b) shows TEM images of the SiMCM-41 and $Ti_{30}Si_{70}$MCM-41 samples. The hexagonal array of the nanoporous materials can be observed clearly with an electronic beam passing through both the parallel and vertical axes of the channels, which further evidences the highly ordered hexagonal structure [27]. This ordered structure was disturbed when 30 mol% Ti ions were introduced and the pores became slightly larger. This confirms that the incorporation of Ti ions disrupts the Si-O framework and weakens its integrity, although pore collapse was generally not observed with Ti insertion. These observations well match the XRD results. The EDX results identified the presence of metals on the surface of $Ti_{30}Si_{70}$MCM-41, as illustrated in Fig. 3, and the table on the bottom right shows the atomic composition determined by EDX. The Ti/Si atomic molar ratio in the sample was 4.86 (ideal value=4.29), which did not appear to be perfectly quantitative. Although it is a very good surface analytical method, EDX is prone to error because the composition may vary according to the location. In particular, the variation is large when the sample is nonuniform. Alternatively, an elemental mapping image shows the spatial distribution of elements in a sample, and the EDX mapping images for the $Ti_{30}Si_{70}$MCM-41 sample in this study revealed the presence and the distributions of O, Si, and Ti.

2. CO_2 Photoreduction over N_{719}-photosensitized $Ti_{30}Si_{70}$MCM-41

Generally, CH_4 production via CO_2 reduction with H_2O can be divided into three sub-processes [28]: proton production through

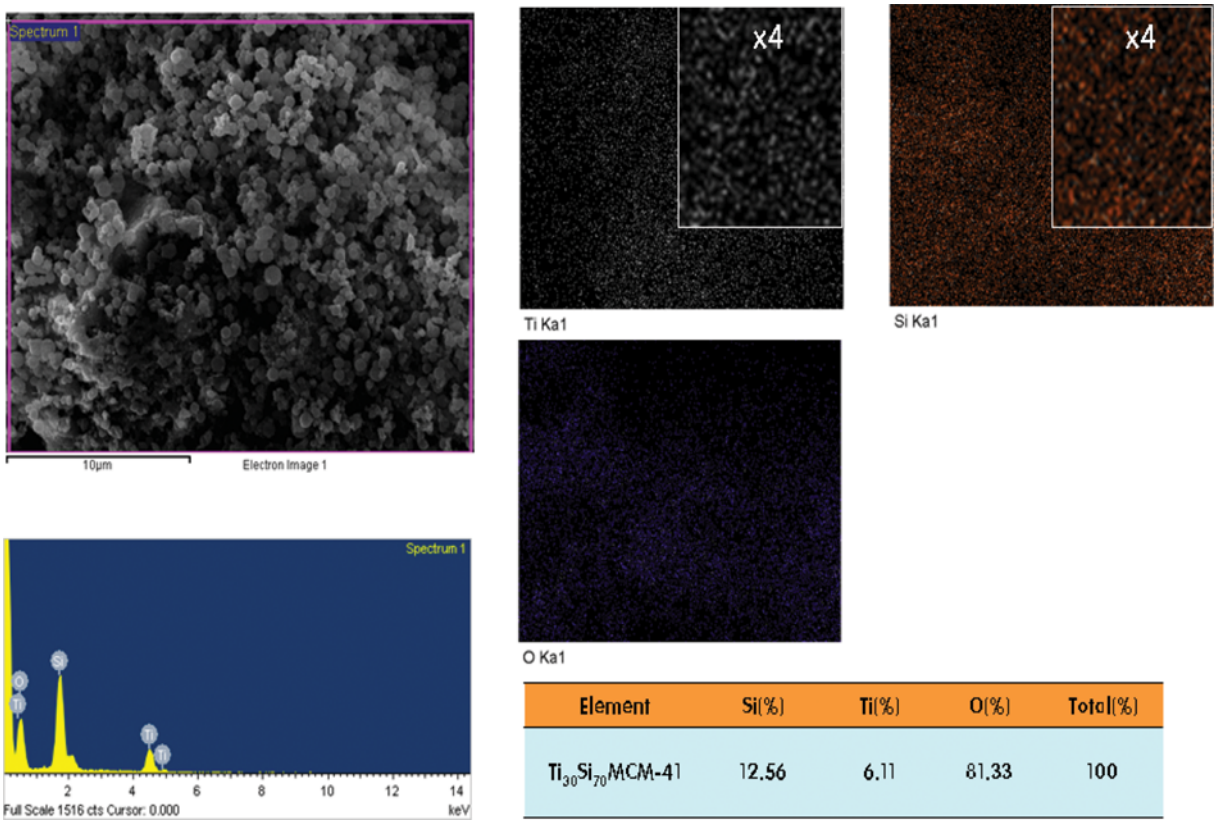

Element	Si(%)	Ti(%)	O(%)	Total(%)
$Ti_{30}Si_{70}$MCM-41	12.56	6.11	81.33	100

Fig. 3. Energy-dispersive X-ray spectra of $Ti_{30}Si_{70}$MCM-41.

H_2O photodecomposition, CO radical production through CO_2 photocleavage, and methane production through photosynthesis between the CO radical and proton. The electrons photogenerated on the photocatalysts by UV radiation induce CO_2 reduction to generate $CO_2^{\bullet}$ radicals, whereas the holes react with the adsorbed H_2O molecules to induce oxidation. The intermediate photogenerated species undergo different reactions to generate CO and CH_4. The production of CH_4 from methyl radicals ($^{\bullet}CH_3$) has been confirmed, and these radicals are directly dependent on the formation of the intermediate product, CO. This reaction summary confirmed that hydrocarbons could be produced by photocatalysts with good reduction potentials. Fig. 4(a) shows the photore-

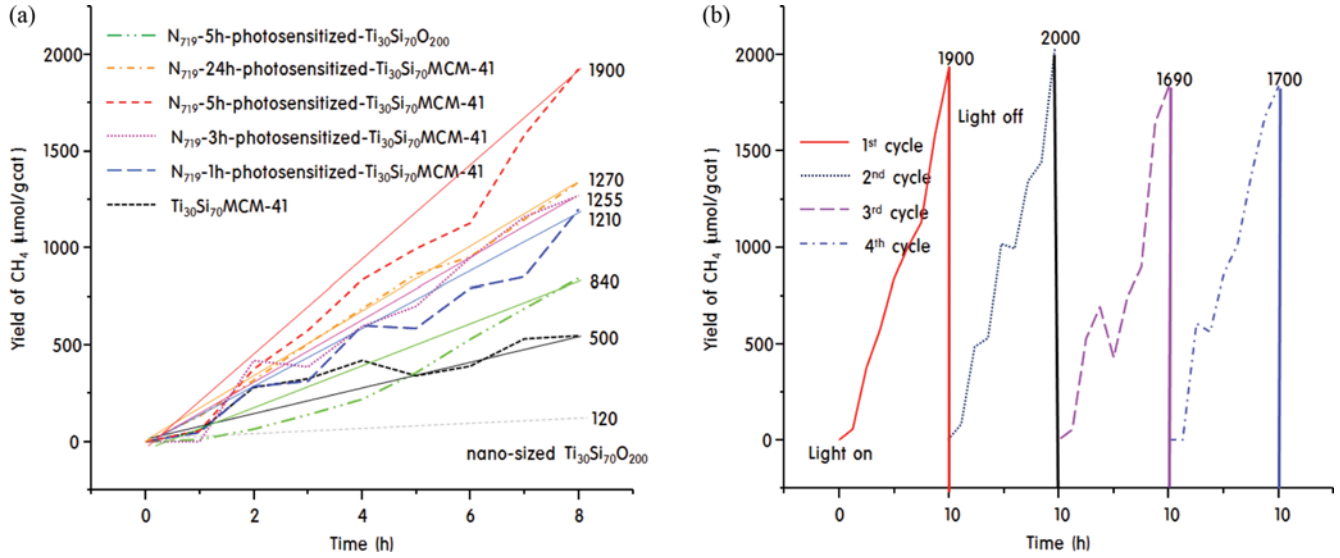

Fig. 4. Photoreduction of CO_2 with H_2O vapor to CH_4 over the N_{719}-x h (x=1, 3, 5, and 24)-photosensitized $Ti_{30}Si_{70}$MCM-41 catalysts (a) and the recycling test for The N_{719}-(5 h)-photosensitized $Ti_{30}Si_{70}$MCM-41 catalyst (b).

duction of CO_2 with H_2O vapor to CH_4 over the N_{719}-(x h)-photosensitized $Ti_{30}Si_{70}$MCM-41 catalysts (x=1, 3, 5, and 24). Almost no methanol and formic acid was observed, but about one-third of methane was found in CO. As the methane increased, carbon monoxide also increased while maintaining the ratio of 3 : 1. Therefore, we focused on the amount of methane. Higher N_{719} adsorption onto the $Ti_{30}Si_{70}$MCM-41 surface led to higher photoactivity in CO_2 photoreduction. Only 550 μmol g_{cat}^{-1} L^{-1} CH_4 was emitted over non-dye-photosensitized $Ti_{30}Si_{70}$MCM-41, but the production increased gradually with increasing N_{719} adsorption time. The maximum CH_4 yield was 1,900 μmol g_{cat}^{-1} L^{-1} over the N_{719}-(5 h)-photosensitized $Ti_{30}Si_{70}$MCM-41 catalyst after 8 h, compared to 840 μmol g_{cat}^{-1} L^{-1} obtained using the N_{719}-(5 h)-photosensitized $Ti_{30}Si_{70}O_{200}$ nanocatalyst (reference material, anatase structure, hydrothermal synthesis, 20-30 nm particle size, 192.0 m^2 g^{-1} specific surface area). On the other hand, the yield was much lower with the more dye-adsorbed N_{719}-(24 h)-photosensitized $Ti_{30}Si_{70}$MCM-41 catalyst, probably because of the poor electron transfer between the dyes and the clogged pores due to the irregular arrangement between many dye molecules. These results demonstrated the great effects of the nanopores in the photoreaction and the importance of the optimal amount of adsorbed dye. The N_{719}-(5 h)-photosensitized $Ti_{30}Si_{70}$MCM-41 catalyst shows excellent performance stability in a recycling test as shown in Fig. 4(b). For this purpose, the catalyst was washed with methanol after the reaction for 10 h, then dried under vacuum and reused for the next run. As results show, there is no significant loss of photocatalytic activity even after four cycles, which shows that the most of adsorbed species were only adsorbed physicochemically.

According to the CO_2 photoreduction mechanism, in the first step, water and CO_2 gases are adsorbed on the surface of the photocatalysts, which initiates the photoreduction reaction [29]. Therefore, the photocatalytic performance depends on adsorption capacities of these two gases, which are injected from outside the reactor. We determined the CO_2 adsorption ability for the two samples: nanoporous $Ti_{30}Si_{70}$MCM-41 and non-porous $Ti_{30}Si_{70}O_{200}$. The CO_2 adsorption profiles were obtained at high temperatures (>900 °C), corresponding to CO_2 desorption on metal oxide species, as shown in Fig. 5. The curve intensity increased significantly for the $Ti_{30}Si_{70}$MCM-41 sample, indicating that considerably more CO_2 molecules were adsorbed on the surface of the exposed Si-O-Ti in the $Ti_{30}Si_{70}$MCM-41 framework. In general, a rapid catalytic reaction happens when many reactants are well adsorbed over the catalyst. The presence of nanopores most likely caused a relative increase in the adsorption of CO_2 molecules.

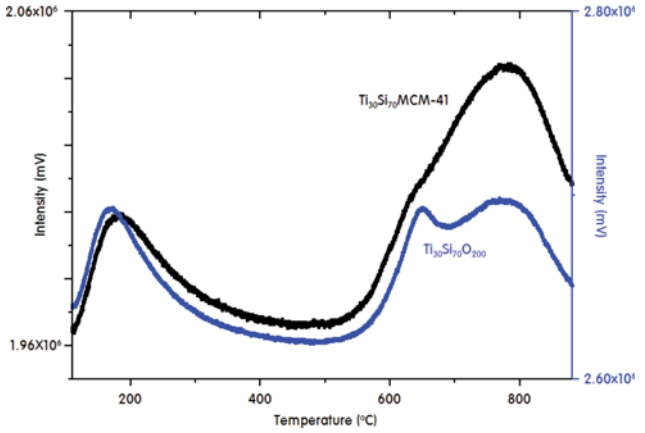

Fig. 5. CO_2-TPD curves corresponding to CO_2 desorption on the $Ti_{30}Si_{70}$MCM-41 and $Ti_{30}Si_{70}O_{200}$ samples.

Table 1. BET surface areas of $Ti_{30}Si_{70}$MCM-41 and $Ti_{30}Si_{70}O_{200}$

	BET multipoint surface area (m^2/g)	Total pore volume (cm^3/g)	Pore size (nm)
$Ti_{30}Si_{70}$MCM-41	541.39	0.3571	1.1
$Ti_{30}Si_{70}O_{200}$	191.88	0.3017	10.7

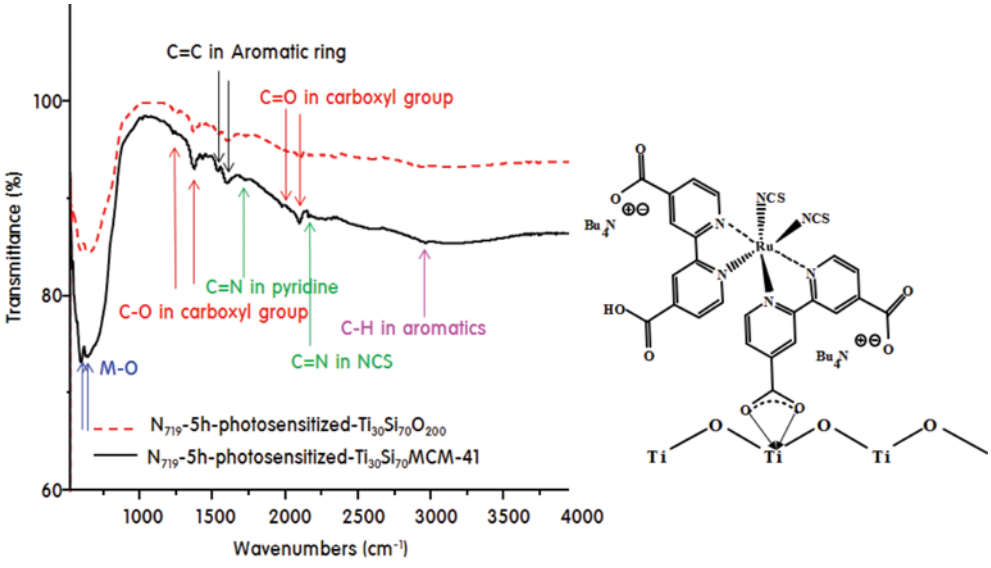

Fig. 6. FT-IR spectra of $Ti_{30}Si_{70}$MCM-41 and $Ti_{30}Si_{70}O_{200}$ samples after dye absorption.

Moreover, the result in Fig. 5 is in good agreement with the measured BET surface areas of $Ti_{30}Si_{70}$MCM-41 and $Ti_{30}Si_{70}O_{200}$, which are 541 and 192 $m^2 g^{-1}$, respectively, as shown in Table 1.

3. Optical and Chemical Properties of the N_{719}-photosensitized $Ti_{30}Si_{70}$MCM-41 Catalyst

Fig. 6 shows the FT-IR spectra of $Ti_{30}Si_{70}$MCM-41 and $Ti_{30}Si_{70}O_{200}$ powders after dye adsorption to observe the interfacial binding energy between the dye molecules (N719) and the film surface. The absorptions around 2,250 and 1,640-1,690 cm^{-1} belong to the SCN and C=N stretching bonds in the pyridine ring. The IR spectra show absorption at 1,000-1,300 and 1,700-1,725 cm^{-1}, which belong to the C-O and C=O stretching modes in the carboxyl group. The C=C and C-H stretching modes in the aromatic rings are at approximately 1,450-1,650 and 2,800-3,050 cm^{-1}, respectively [30]. The intensities of the IR modes are stronger in the $Ti_{30}Si_{70}$MCM-41 than in the $Ti_{30}Si_{70}O_{200}$. Furthermore, when a dye molecule is linked with metal in a semiconductor, bi-dentate coordination occurs between them [31]. The IR spectrum of the $Ti_{30}Si_{70}$MCM-41 shows a strong band at 500 cm^{-1}, which belongs to metal-O group due to a new Ti-O bond between O of COO^- and Ti or Si atom, which is relatively weaker over the $Ti_{30}Si_{70}O_{200}$. Therefore, the connection between the $Ti_{30}Si_{70}$MCM-41 and dye molecule is stable due to a bidentate linkage than $Ti_{30}Si_{70}O_{200}$, which led to an increase of the CO_2 photoreduction due to the better transport of electrons.

Fig. 7 shows the diffuse reflectance UV-vis absorption spectra of the N_{719}-(x h)-photosensitized $Ti_{30}Si_{70}$MCM-41 catalysts with different dye adsorption durations. All samples show two maximum bands located in the 250-400 nm region, suggesting that the polymerized Ti-O-Ti species have higher coordination, such as with hexahedral or tetrahedral coordinated Ti(IV) species (possibly the tetrahedral positions in the nanoporous framework), and the 450-650 nm region, which was assigned to N_{719} dye absorption. UV-vis spectroscopy shows that the Ti atoms entered the silica framework and that no additional titanium framework was formed during the microwave irradiation synthesis. In addition, the absorption intensity increased depending on the dye adsorption times. On the other hand, the absorption spectra show steeper absorption edges; this is similar to the HOMO-LUMO gap results that were estimated by using Tauc's equation [32]. The estimated HOMO-LUMO gaps of pure $Ti_{30}Si_{70}$MCM-41, and $Ti_{30}Si_{70}$MCM-41 and N_{719} in the N_{719}-(5 h)-photosensitized $Ti_{30}Si_{70}$MCM-41 catalyst were 3.1 (400 nm), 2.92 (425 nm), and 1.70 (730 nm) eV, respectively. The HOMO-

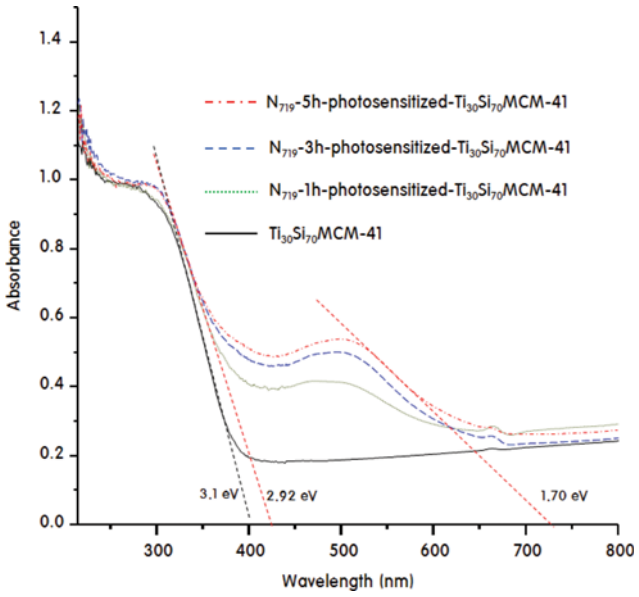

Fig. 7. Diffuse reflectance-UV-visible absorption spectra of the N_{719}-x h-photosensitized $Ti_{30}Si_{70}$MCM-41 catalysts according to the dye adsorption times.

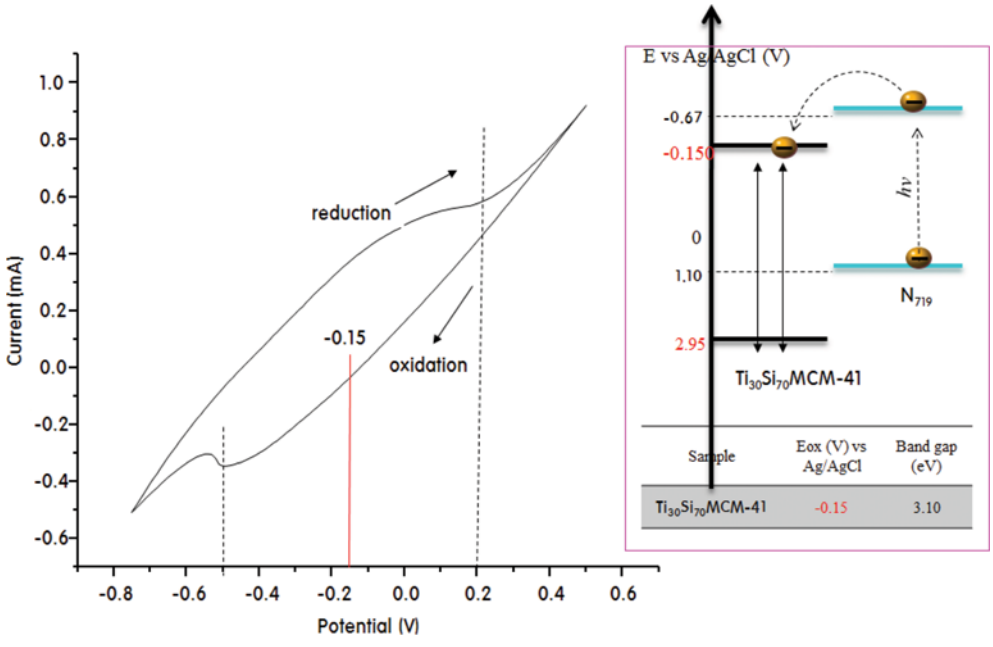

Fig. 8. Cyclic voltammogram of $Ti_{30}Si_{70}$MCM-41.

LUMO gaps and band heights decreased with increasing N_{719} adsorption time. Although a lower HOMO-LUMO gap is generally better for enhancing the photocatalytic performance under weak solar radiation, this improvement can be negated by the smaller band gap that is available to facilitate recombination between the electrons and holes [33]. On the other hand, as shown in the right figure, the carbonate groups of the N_{719} dye are bidentate-linked to Ti atoms in the porous Ti oxide framework [34]. In particular, the bond between COO^- and the surface of the nanoporous TiO_2 is strong owing to the perfect bidentate linkage. On the other hand, the bonding is not significant on nanosized TiO_2. This suggests that coordination of the N_{719} dye on nano-sized TiO_2 is mainly attributable to the contributions of a monodentate and bidentate linkage. Therefore, the nanoporous TiO_2 film has a better surface morphology for a bidentate linkage than nanosized TiO_2 has, which enhances the photocatalytic performance owing to easier electron transport.

Fig. 8 shows cyclic voltammograms of $Ti_{30}Si_{70}$MCM-41. A reversible wave for the absolute potentials between the reduction (E_{pa}) and oxidation peaks (E_{pc}) is credible. The potential wave for for $Ti^{4+} \leftrightarrow Ti^0$ in the $Ti_{30}Si_{70}$MCM-41 sample was reversible, and the midpoint potential is approximately E_{mid}=−0.15 V vs. Ag/AgCl (3 M KCl). In addition to the band gap, the potential locations of the valence and conduction bands of $Ti_{30}Si_{70}$MCM-41 are important. The energy levels of the highest occupied molecular orbital (HOMO) and LUMO can be determined using CV equations (under V vs. normal hydrogen electrode or eV vs. vacuum) [35]. The HOMO (or valence band) potential of the samples can be obtained easily from the LUMO and the band gap. The calculated HOMO for $Ti_{30}Si_{70}$MCM-41 was +2.95 V. From the previously reported band gap, HOMO, and LUMO energies for the N_{719} dye [36], a potential energy diagram between the N_{719} dye and $Ti_{30}Si_{70}$MCM-41 can be drawn, as shown in the right figure. The superior photocatalytic conversion of N_{719}-photosensitized $Ti_{30}Si_{70}$MCM-41, compared to that of $Ti_{30}Si_{70}$MCM-41, is attributed to the increased absorption of visible light induced by the N_{719} dye. The figure shows that the first electronic transition occurs easily in the N_{719} dye owing to radiation, and the electrons at a higher LUMO in the N_{719} dye then move to the $Ti_{30}Si_{70}$MCM-41 conduction band, whereas the hole in $Ti_{30}Si_{70}$MCM-41 moves to the HOMO of the N_{719} dye, which is formed by the recycling of the current. Therefore, their recombination of excited electrons and holes is suppressed during photocatalysis, and the rate of CO_2 photoreduction is eventually enhanced.

The efficiencies of photogenerated electron-hole production in $Ti_{30}Si_{70}$MCM-41, N_{719}-(5 h)-photosensitized $Ti_{30}Si_{70}$MCM-41, and N_{719}-(5 h)-photosensitized $Ti_{30}Si_{70}O_{200}$ films were measured through the photocurrent response under solar light radiation. Fig. 9 presents the typical real-time photocurrent responses of the three films when the light source is switched on and off; the rapid rise and decay of the photocurrent is clearly shown. In semiconductor systems, when radiation provides more energy than the band gap of a semiconductor does, the electrons are excited from the valence band to the conduction band, leaving behind a hole in the valence band, and this electron-hole pair is responsible for the photocurrent. When the light is turned on, a rapid increase in photoreduction current is observed, and the photocurrent then stabilizes to a steady state after a few seconds. When the light is turned off, the photocurrent decreases instantaneously to nearly zero [37]. In our study, the maximum photocurrent of the N_{719}-(5 h)-photosensitized $Ti_{30}Si_{70}$MCM-41 film when the light was turned on was 100 μA cm^{-2}, which was four and two times higher than those achieved on the $Ti_{30}Si_{70}$MCM-41 (25 μA cm^{-2}) and N_{719}-(5 h)-photosensitized $Ti_{30}Si_{70}O_{200}$ (50 μA cm^{-2}) films, respectively. This increment reveals a lower level of electron-hole recombination in N_{719}-(5 h)-photosensitized $Ti_{30}Si_{70}$MCM-41. On the other hand, the transient photocurrents were rapid, steady, prompt, and reproducible over several on-off switching cycles of the visible light radiation for $Ti_{30}Si_{70}$MCM-41 and N_{719}-(5 h)-photosensitized $Ti_{30}Si_{70}O_{200}$. No overshoots were observed at the beginning and end of the flash. The rectangular response reveals the absence of any grain boundaries in the direction of electron diffusion. Such grain boundaries create deep traps that hinder electron transport and may exist at the particulate electrode [38]. On the other hand, the currents in both the light-on and light-off regions in N_{719}-(5 h)-photosensitized $Ti_{30}Si_{70}$MCM-41 increased as time increased, which indicates the presence of grain boundaries due to the nanopore framework and, further, implies efficient flow of excited electrons in the external circuit. Therefore, the nanopores and dye both have beneficial effects on the photocurrent; they facilitate the efficient separation of photogenerated hole-electron pairs and the effective movement of excited electrons.

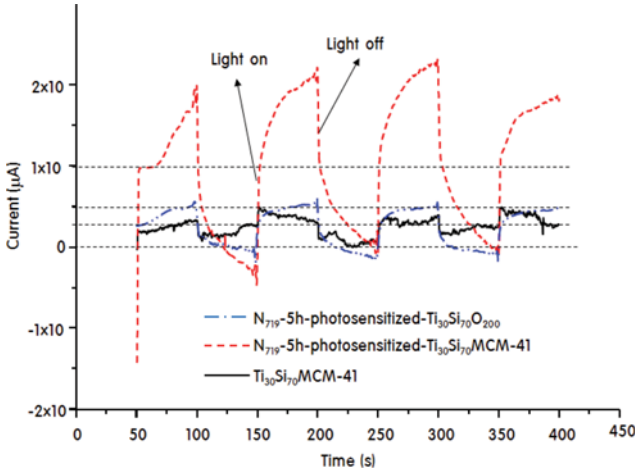

Fig. 9. Photocurrent responses under solar light irradiation at an applied potential of 0.7 V vs. SCE for $Ti_{30}Si_{70}$MCM-41, N_{719}-5 h-photosensitized $Ti_{30}Si_{70}$MCM-41, and N_{719}-5h-photosensitized $Ti_{30}Si_{70}O_{200}$ films.

CONCLUSIONS

Based on the relationships between the optical properties of photocatalysts and their catalytic activities, we have proposed a model for CO_2 photoreduction over N_{719}-(5 h)-photosensitized $Ti_{30}Si_{70}$MCM-41, as shown in Scheme 1. Photon excitation in N_{719} over N_{719}-(5 h)-photosensitized $Ti_{30}Si_{70}$MCM-41 begins rapidly owing to its very small band gap, and the electrons are partially released into the conduction band of $Ti_{30}Si_{70}$MCM-41. However, some electrons can also be transferred efficiently to CO_2 molecules over the

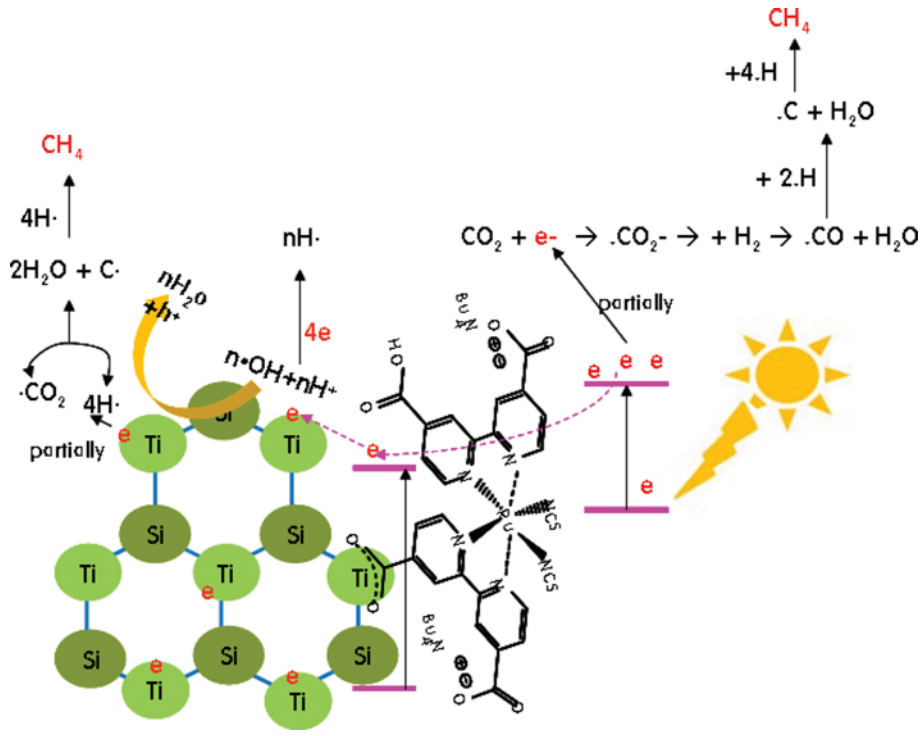

Scheme 1. Model for CO_2 photoreduction over N_{719}-photosensitized $Ti_{30}Si_{70}$MCM-41.

dye. The positive holes on the $Ti_{30}Si_{70}$MCM-41 valence band can be trapped by H_2O and then transferred to OH radicals and protons. The obtained protons are transformed by electrons into H radicals, which in turn react with C and CO radicals to afford $CO_2^{\bullet}$, and hence generate CH_4. These processes promote the separation of photogenerated electron-hole pairs (e^-/h^+) in the photocatalyst to accelerate the CO_2 reduction process. Therefore, the synergistic effects of the nanopores and dye in N_{719}-photosensitized $Ti_{30}Si_{70}$MCM-41 enhance CO_2 reduction.

ACKNOWLEDGEMENTS

This work was supported by the Human Resource Training Program for Regional Innovation and Creativity through the Ministry of Education and National Research Foundation of Korea (NRF-2015H1C1A1035639), for which the authors are very grateful.

REFERENCES

1. S. Baj, T. Krawczyk, A. Dąbrowska, A. Siewniak and A. Sobolewski, *Korean J. Chem. Eng.*, **32**, 2295 (2015).
2. B. Lee and H. Lim, *Korean J. Chem. Eng.*, **34**, 199 (2017).
3. M. Park, B. S. Kwak, S. W. Jo and M. Kang, *Energy Convers. Manage.*, **103**, 431 (2015).
4. K. Li, T. Peng, Z. Ying, S. Song and J. Zhang, *Appl. Catal. B Environ.*, **180**, 130 (2016).
5. M. Anpo, *J. CO_2 Utiliz.*, **1**, 8 (2013).
6. Z. Xiong, H. Wang, N. Xu, H. Li, B. Fang, Y. Zhao, J. Zhang and C. Zheng, *Int. J. Hydrogen. Energy*, **40**, 10049 (2015).
7. O. Ola and M. Mercedes Maroto-Valer, *Appl. Catal. A Gen.*, **502**, 114 (2015).
8. B. Milicevic, V. ĐorCevic, D. Loncarevic, S. P. Ahrenkiel, M. D. Dramicanin and J. M. Nedeljkovic, *Micropor. Mesopor. Mater.*, **217**, 184 (2015).
9. S. Bai, H. Liu, J. Sun, Y. Tiana, S. Chen, J. Song, R. Luo, D. Li, A. Chen and C.-C. Liu, *Appl. Surf. Sci.*, **338**, 61 (2015).
10. Y.-Y. Xu, S.-Q. Lu, Y.-Z. Zheng, H.-B. Fang, X. Tao and J.-F. Chen, *Catal. Commun.*, **69**, 63 (2015).
11. L. Collado, P. Jana, B. Sierra, J. M. Coronado, P. Pizarro, D. P. Serrano and V. A. de la Peña O'Shea, *Chem. Eng. J.*, **224**, 128 (2013).
12. J. Belosevic-Cavor, K. Batalovic, V. Koteski, J. Radakovic and C. M. Rangel, *Int. J. Hydrogen. Energy*, **40**, 9696 (2015).
13. K.-J. Hwanga, Y. Jeong, C. Choi, Y. J. Kim, G. Kim, Y.-K. Choi, S. Jina and D.-W. Park, *Nano Energy*, **16**, 383 (2015).
14. J. Zhang, Y. Rui, Y. Li, Q. Zhang and H. Wang, *Electrochimica Acta*, **176**, 480 (2015).
15. G. Benkö, J. Kallioinen, J. E. I. Korppi-Tommola, A. P. Yartsev and V. Sundström, *J. Am. Chem. Soc.*, **124**, 489 (2002).
16. S. Füldner, R. Mild, H. I. Siegmund, J. A. Schroeder, M. Gruber and B. König, *Green Chem.*, **12**, 400 (2010).
17. F. Theil, A. Dellith, J. Dellith, A. Undisz, A. Csaki, W. Fritzsche, J. Popp, M. Rettenmayr and B. Dietzek, *J. Colloid Interface Sci.*, **421**, 114 (2014).
18. M. S. Sadjadi, N. Farhadyar and K. Zare, *Superlattice. Microst.*, **46**, 266 (2009).
19. S. Shen and L. Guo, *Catal. Today*, **129**, 414 (2007).
20. L. Yu, X. Yang and D. Wang, *J. Colloid Interface Sci.*, **448**, 525 (2015).
21. S. W. Jo, B. S. Kwak, K. M. Kim, J. Y. Do, N.-K. Park, S. O. Ryu, H.-J. Ryu, J.-I. Baek and M. Kang, *Appl. Surf. Sci.*, **355**, 891 (2015).
22. C. Dong, M. Xing and J. Zhang, *J. Phys. Chem. Lett.*, **7**, 2962 (2016).

23. M. Xing, F. Shen, B. Qiu and J. Zhang, *Sci. Rep.*, **4**, 6341 (2014).
24. Y. Shu, Y. Shao, X. Wei, X. Wang, Q. Sun, Q. Zhang and L. Li, *Micropor. Mesopor. Mater.*, **214**, 88 (2015).
25. P. Fu, T. Yang, J. Feng and H. Yang, *J. Ind. Eng. Chem.*, **29**, 338 (2015).
26. L. Martins, W. Hölderich, P. Hammer and D. Cardoso, *J. Catal.*, **271**, 220 (2010).
27. L. Li, P. Wu, Q. Yu, G. Wu and N. Guan, *Appl. Catal., B: Environ.*, **94**, 254 (2010).
28. Y. Li, W.-N. Wang, Z. Zhan, M.-H. Woo, C.-Y. Wu and P. Biswas, *Appl. Catal. B: Environ.*, **100**, 386 (2010).
29. Ş. Neaţu, J. Antonio Maci-Agull and H. Garcia, *Int. J. Mol. Sci.*, **15**, 5246 (2014).
30. A. Alparone, *Spectrochim. Acta Part A*, **81**, 631 (2011).
31. J. Y. Do, Y. Im, B. S. Kwak and M. Kang, *J. Ind. Eng. Chem.*, **34**, 89 (2016).
32. A. Tumuluri, K. Lakshun Naidu and K. C. James Raju, *J. Chem. Tech. Res.*, **6**, 3353 (2014).
33. F. A. Rustamov, N. H. Darvishov, V. E. Bagiev, M. Z. Mamedov, E. Y. Bobrova and H. O. Qafarova, *J. Lumin.*, **154**, 224 (2014).
34. Y. Lee and M. Kang, *Mater. Chem. Phys.*, **122**, 284 (2010).
35. J. H. Kim and H. Lee, *Synth. Met.*, **139**, 471 (2003).
36. S. Gubbala, V. Chakrapani, V. Kumar and M. K. Sunkara, *Adv. Funct. Mater.*, **18**, 2411 (2008).
37. S. S. Kalanur, Y. J. Hwang and O.-S. Joo, *J. Colloid Interface Sci.*, **402**, 94 (2013).
38. M. Sookhakian, Y. M. Amin, S. Baradaran, M. T. Tajabadi, A. Moradi Golsheikh and W. J. Basirun, *Thin Solid Films*, **552**, 204 (2014).